US Army Corps
of Engineers®
Engineer Research and
Development Center

ERDC
INNOVATIVE SOLUTIONS
for a safer, better world

Strategic Environmental Research and Development Program (SERDP)

Munition Penetration-Depth Prediction

SERDP SEED Project MR-2629

Arnold J. Song, Brendan A. West, Oliver-Denzil S. Taylor,
Devin T. O'Connor, Matthew D. Parno, Taylor S. Hodgdon,
David M. Cole, and Jay L. Clausen

August 2017

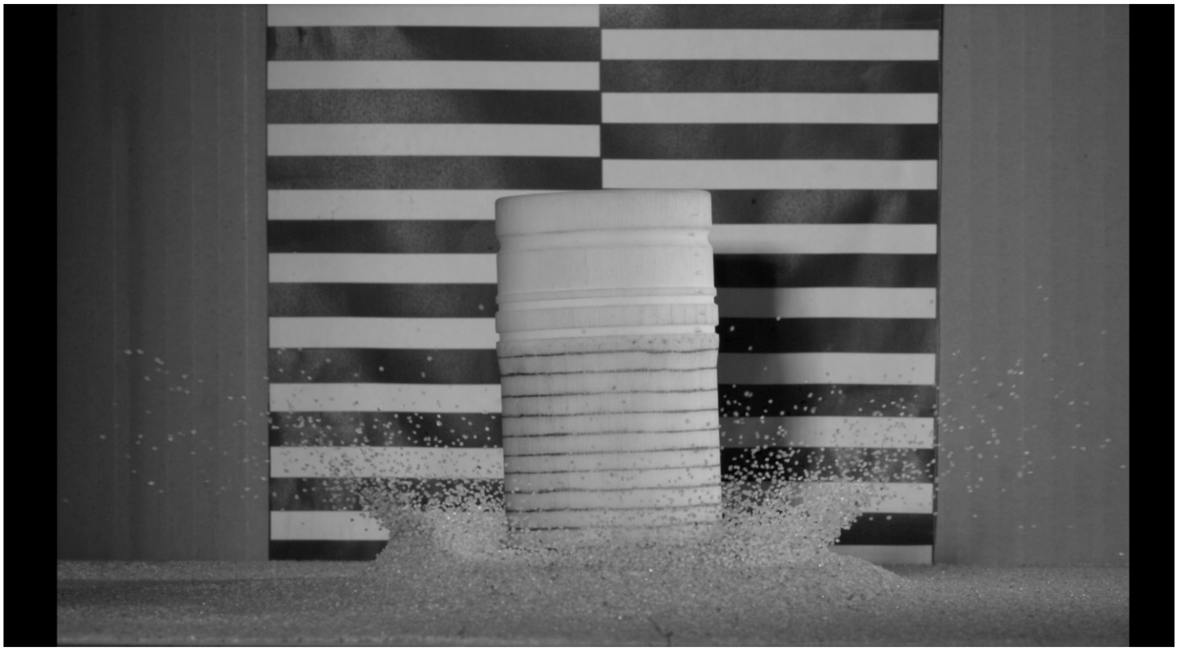

Cold Regions Research
and Engineering Laboratory

Strategic Environmental Research and
Development Program (SERDP)

ERDC/CRREL TR-17-12
August 2017

Munition Penetration-Depth Prediction

SERDP SEED Project MR-2629

Arnold J. Song, Brendan A. West, Oliver-Denzil S. Taylor, Devin T. O'Connor,
Matthew D. Parno, Taylor S. Hodgdon, David M. Cole, and Jay L. Clausen

U.S. Army Engineer Research and Development Center (ERDC)
Cold Regions Research and Engineering Laboratory (CRREL)
72 Lyme Road
Hanover, NH 03755-1290

Final Report

Prepared for Strategic Environmental Research and Development Program (SERDP)
4800 Mark Center Drive, Suite 17D08
Alexandria, VA 22350-3605

Under SEED Project MR-2629, "Munition Penetration-Depth Prediction"

Abstract

Existing models for predicting the penetration depth of munitions and explosives of concern are inaccurate and insufficient from a user (range manager, U.S. Army Corps of Engineers project manager, or environmental consultant) operability perspective for current needs. We attribute poor model performance to (1) a heavy dependence on empirically derived parameterizations poorly linked to the physical properties of the target material or (2) physics-based models that inadequately capture the salient mechanical processes, especially in the first meter of penetration. Consequently, we have developed a micromechanical-based model using a hybrid discrete element model (DEM) / finite element model (FEM) approach capable of a detailed treatment of near-surface soil properties. To examine the effects of varying levels of moisture on the dynamic behavior of a soil, we fabricated a small-scale triaxial shear test to inform the development and calibration of the DEM contact model. We conducted projectile-drop tests into sand with a scale version of a 57 mm projectile and measured projectile penetration to compare with model results.

Contents

Report Documentation Page

Figures and Tables

Figures

Tables

Preface

This study was conducted for Strategic Environmental Research and Development Program (SERDP) under SEED Project MR-2629, “Munition Penetration-Depth Prediction.” The technical monitor was Mr. Herbert Nelson, SERDP.

The work was performed by the Biogeochemical Sciences Branch (CEERD-RRN) of the Research and Engineering Division (CEERD-RR), U.S. Army Engineer Research and Development Center, Cold Regions Research and Engineering Laboratory (ERDC-CRREL). At the time of publication, Dr. Justin Berman was Chief, CEERD-RRN, and CDR J. D. Horne, USN (Ret), was Chief, CEERD-RR. The Deputy Director of ERDC-CRREL was Dr. Lance Hansen, and the Director was Dr. Joseph L. Corriveau.

The authors would like to acknowledge Mr. H. Nelson and the Strategic Research and Environmental Development Program for providing funding for this SEED project.

COL Bryan S. Green was Commander of ERDC, and Dr. David W. Pittman was the Director.

Acronyms and Abbreviations

ASTM	American Society for Testing and Materials
CRREL	Cold Regions Research and Engineering Laboratory
DEM	Discrete Element Model
ERDC	U.S. Army Engineer Research and Development Center
FEM	Finite Element Model
MEC	Munitions and Explosives of Concern
SERDP	Strategic Environmental Research and Development Program
USACE	U.S. Army Corps of Engineers

Executive Summary

Objectives

Existing models for predicting penetration depth of munitions and explosives of concern (MEC) are inaccurate and insufficient from a user (range manager, U.S. Army Corps of Engineers (USACE) project manager, or environmental consultant) operability perspective for current needs. We attribute poor model performance to (1) a heavy dependence on empirically derived parameterizations poorly linked to the physical properties of the target material or (2) physics-based models that inadequately capture the salient mechanical processes, especially in the first meter of penetration. To address these shortcomings our objective is to develop improved constitutive behavior models by using a micromechanical approach that explicitly accounts for material properties such as soil moisture content, grain size, shape, and density.

Technical Approach

Our technical approach involves the development of a micromechanical-based model using a hybrid discrete element model (DEM) / finite element model (FEM) capable of a detailed treatment of near-surface soil properties. DEM model particle configurations were generated from three-dimensional microCT imaging of a soil sample. To examine the effects of varying levels of moisture on the dynamic behavior of a soil, we fabricated a small-scale triaxial shear test to inform the DEM contact model development and calibration. Projectile-drop tests into sand were conducted with a scale version of a 57 mm projectile where we measured projectile penetration for comparison with model results.

Results

An improved constitutive model framework has been developed that improves projectile penetration by relying only on the parent material characteristics (elastic modulus, Poisson's ratio), grain geometry, friction coefficient, and the volume of pore water. Of these parameters, the friction coefficient is the least known for a particular soil type. The triaxial shear test experiments, which characterize the dynamic behavior and transfer of energy through the soil fabric, serve as a good source of data to calibrate the friction coefficient. The preliminary numerical model results compare well in a qualitative sense with the drop-test measurements.

Benefits

Application of these improved constitutive soil behavior models allows for probability estimates of specific munition types to the depth of interest that will lead to accurate time and cost projections of MEC cleanup during project planning. This will provide the MEC recovery team with tighter bounds on the uncertainty associated with apparent MEC at depth identified during geophysical surveys and will limit the over-excavation of apparent MEC at depth, thus reducing the Department of Defense cleanup costs for the Formerly Used Defense Sites and Base Realignment and Closure sites under the Military Munition Response Program.

1 Introduction

1.1 Background

Over 4900 munitions testing sites in the United States will require a combined total of $13 billion of remediation efforts over the following decades to remove munitions and explosives of concern (MEC). The munitions-range managers, U.S. Army Corps of Engineers (USACE) project managers, and environmental consultants tasked with these remediation efforts have several tools at their disposal to detect or estimate the depth of MEC, including geophysical sensors and physics-based numerical models. Although these tools have reduced remediation costs significantly, their current depth-prediction capabilities are lacking. Physics-based models are unable to capture the important mechanical process of penetration, especially within 1 m of the ground's surface, and rely heavily on empirical parameterizations that poorly describe the target materials' physical properties. The uncertainty associated with these methods can lead to inflated time and cost estimates for MEC cleanup.

1.2 Objectives

This study was funded by the Strategic Environmental Research and Development Program (SERDP) and was conducted in support of the FY17 SERDP SEED call for proposal. The goal of this study was to address these shortcomings by developing improved constitutive behavior models from a micromechanical approach that explicitly accounts for material properties such as soil moisture content, grain size, shape, and density. Applying these improved constitutive soil behavior models allows for probability estimates of specific munition types to the depth of interest and will lead to accurate time and cost projections of MEC cleanup during project planning. This will provide the MEC recovery team with tighter bounds on the uncertainty associated with apparent MEC at depth identified during geophysical surveys and will limit the overexcavation of apparent MEC at depth, thus reducing the Department of Defense cleanup costs for the Formerly Used Defense Sites and Base Realignment and Closure sites under the Military Munition Response Program.

1.3 Approach

Our technical approach involved developing a micromechanical-based model using a hybrid discrete element model (DEM) / finite element model (FEM) capable of a detailed treatment of near-surface soil properties. DEM model particle configurations were generated from three-dimensional microCT imaging of a soil sample. To examine the effects of varying levels of moisture on the dynamic behavior of a soil, we fabricated a small-scale triaxial shear test to inform the DEM contact model development and calibration. Projectile-drop tests into sand were conducted with a scale version of a 57 mm projectile where we measured projectile penetration for comparison with model results.

2 Fundamental Theory

2.1 Penetration dynamics

The dynamics of a projectile penetrating a target medium is a function of the projectile geometry, projectile impact energy, target material properties, and the contact mechanics between the projectile and the target material. Previous studies have primarily explored the penetration-dynamics problem, ultimately to estimate penetration trajectory and depth, as a cavity-expansion problem where the projectile pushes the target material out of the way to create the cavity that the projectile then occupies. This strain due to cavity formation induces stresses on the cavity boundary (i.e., the projectile–soil interface) that act normal (cavity pressure) and tangentially (friction between projectile and target material) to the projectile surface, decelerating the body as it moves through the target medium (Bless et al. 2012; Borg et al. 2012). This deceleration can be described generally as

$$-\frac{dv}{dt} = \alpha v^2 + \beta v + \gamma \tag{1}$$

where α, β, and γ are empirically determined constants, as with Young's equations (Young 1967, 1997), or are obtained using a physics-based approach that uses cavity expansion theory (e.g., the work from Forrestal et al. 1992 and more recently Shi et al. 2014).

There are two commonly used simplifications of the general penetration equation: (1) the Robins-Euler simplification that assumes the projectile deceleration is velocity independent, therefore $\alpha = 0$ and $\beta = 0$, and (2) the Poncelet equation where $\beta = 0$ and α and γ are nonzero positive constants. The Robins-Euler equation applies to low velocity impacts where the boundary location between plastic and elastic deformation regions remains nearly constant for the velocity range of interest because the stress front propagates much more quickly than the projectile. As the projectile impact velocity increases, the cavity pressure begins to exhibit velocity dependence; and the deceleration function takes the form that Poncelet posits. This form of the general penetration equation is the one that is typically used to derive the empirical and physics-based penetration-depth equations.

Several researchers have attempted to empirically correlate the cavity pressure to the projectile impact velocity and geometry based on penetration-depth experiments (Young 1967, 1997; Bernard 1977, 1978; Bernard and Creighton 1978, 1979; Allen et al. 1957). These relationships are not physics based and require well-characterized experiments to characterize the soil's penetrability index, or S-number. The generality of these empirically based correlations is limited or nonexistent and would require a vast database of experiments to account for variations in soil type, stratigraphy, and moisture content. In addition, a statistical picture of the penetration depth would be impossible with this type of model because of this loose correlation between the soil properties and the parametrization.

2.2 Physics-based penetration models

In contrast to empirical-correlation-based penetration models, physics-based cavity expansion models attempt to determine the cavity pressure, or penetration resistance, according to behavior governed by soil mechanics models, such as the Mohr-Coulomb theory. A fundamental component of cavity-expansion theory is the determination of the propagation velocity of the boundary between the plastically and elastically deforming regions, typically using the yield surface governed by the Mohr-Coulomb or Drucker-Prager failure criterion and assuming that cavity expansion is spherically symmetric. Studies using the spherical cavity expansion approach have accurately predicted penetration depth in porous rock; concrete; and dry, coarse sands (Forrestal et al. 1992; Shi et al. 2014; Forrestal 1986). However, these theories are limited to ogive or conical-nose configurations due to the spherical-symmetry assumption. The DEM approach does not make any of these simplifying assumptions because the particle-to-particle interaction is explicitly described, and bulk properties such as plastic strain are determined a posteriori. The numerical test bed allows us to interrogate the soil sample in ways that are extremely difficult to replicate in physical experiments (e.g., measuring the strain field as the projectile moves through the target medium).

2.2.1 Near-surface soil properties

Soil constitutive modeling is based primarily on Hooke's law of linear elasticity and Coulomb's law of perfect plasticity at small strains ($\varepsilon < 10^{-6}$). Research has shown that soil behavior is complex and nonlinear and exhibits anisotropic time-dependent behavior. This is particularly true in the multiphase continuum mechanics of unsaturated soils in the near surface, the upper 1 m of soil. The soil properties and skeletal structure of the near-surface material will have the greatest influence on penetration depth because these physical properties significantly affect the anisotropic confinement of the soil material. Laboratory investigations (Hardin and Richart 1963; Richart et al. 1970; Hardin and Drnevich 1972; Iwasaki et al. 1974; Tatsuoka et al 1978; Seed et al. 1986) in stress conditions greater than the upper 1 m of overburden have shown that vertical confining stress has the most significant impact on soil state and behavior. Richart et al. (1970) state that the effects of effective confining pressure acting at each point in a soil mass depends on the effective overburden pressures, $\bar{\sigma}_0$, and that compressional and shear wave velocities are dependent on $(\bar{\sigma}_0)^{0.25}$. Therefore, any effect that causes a change in $\bar{\sigma}_0$ also causes a change in wave-propagation velocity, skeletal structure, and ultimately soil behavior. However, the validity of these equations and soil behavior at the near-surface boundary (i.e., the upper 1 m of soil) is not well understood, primarily due to the limited vertical confining stress, the high degree of anisotropy, and the inapplicability of Mohr-Coulomb soil mechanics, which is often ignored or overgeneralized.

2.2.2 Friction coefficient

As described above, the problem of projectile penetration in soil involves significant target material deformation and particle motion in the near field and relatively small deformations (nominally elastic) in the far field. Both of these regions of behavior must be adequately described for accurate penetration-depth estimation. The grain-to-grain friction coefficient, μ, is a key physical quantity that governs the point at which two grains will slide relative to each other and thus establishes the stress conditions under which extensive straining is initiated. Because this condition essentially defines the boundary between near- and far-field behaviors in the soil, μ is a critically important quantity in the present effort. Additionally, the friction between the soil particles and the metal skin of the penetrator is important to the analysis.

Recent work (Cole 2015) has demonstrated with experiments that certain types of naturally occurring grains (generally ones with smooth surfaces, such as river sand or other weathered materials) exhibit a μ that actually decreases with increasing normal force. In some cases, this effect can be quite pronounced, decreasing from approximately 0.8 to 0.2 as the normal force increases from 1 to 20 N. This has the effect of making large-scale (e.g., permanent) strain much easier at high background stress levels and is thus anticipated to be an important effect to include in the penetration model.

3 Materials and Methods

3.1 Discrete element method

Our approach determines mechanical properties of soil in terms of measureable physical properties (particle size, shape, density, and moisture conditions) using a DEM model where the particle-scale mechanics of a soil are explicitly modeled. This physics-based method provides the means to derive a soil's bulk macroscopic properties directly from a micromechanical description of the target material. Modeling the penetration process by using the DEM involves calculating the contact forces and resulting motion for each individual soil grain (for a grain diameter of 1 mm, a meter cubed volume would require approximately 12 million particles), which is very computationally burdensome, to generate robust statistics that require a large number of model realizations. This report describes the preliminary steps to use a DEM method to improve penetration models through the improvement of constitutive models used for soils at the near surface.

We use a mechanistic approach to determine the constitutive behavior of the target material by explicitly describing the interaction between grains composing the target material and the projectile. Our approach takes advantage of the extensive work conducted in recent years by the Engineer Research and Development Center (ERDC), Cold Regions Research and Engineering Laboratory (CRREL), on granular media mechanics and modeling. This approach considers near- and far-field behavior of the soil. The near field is defined as the region of soil subjected to impact loading and large strains. This region requires certain types of submodels to adequately describe the engineering response to energetic loading. The far field is characterized by low strains and involves nominally elastic behavior. Although this is a simpler region to model, its response is still a function of the soil properties and requires a material-specific treatment. Additionally, our previous work (Cole 2015; Cole et al. 2013; Cole and Ketchum 2013; Cole and Peters 2007, 2008) clearly indicates that the location of the boundary between these two regions is determined by the microscale properties of the soil and can be determined a posteriori from the numerical solution.

The proper formulation of the interparticle contact behaviors is important for accurate representation of the bulk properties. For example, the friction coefficient used to calculate the tangential stresses that result from the sliding action at the particle-to-particle interface governs the transition between elastic and plastic deformation of the soil skeleton. The contact equations that are used in the DEM soil model are described below. When two grains are found to be in contact, a plane is placed at the point of contact tangent to the surface of each grain. The force between grains has a component normal to the plane and a tangential component that lies in the plane. The normal and tangential components are calculated from a modified Hertzian model with parallel viscous damping and a Coulomb friction cap on the tangential force. The force components depend on the overlap between dilated grains. The overlap δ between a pair of grains is defined as

$$\delta = |\bar{d}| - 2R < 0 \tag{2}$$

where $\bar{d}$ is the magnitude of the vector that defines the distance between the two undilated grains and R is the dilating radius of grains 1 and 2. Dilation of a polyhedral grain produces a similar polyhedral grain with curved edges and vertices with radii of curvature equal to the dilation radius.

For the normal component of the contact force, we use a Hertzian contact force model similar to the one used by Lin and Ng (1997) that was in turn based on the work of Johnson (1987). The Hertzian model is based on a nonlinear force-displacement relationship that accounts for the increase in contact area between grains as the normal load increases. The Hertzian contact force model was originally developed for spherical grains. The equation for the normal contact force, F_n, as a function of the grain overlap, δ, is

$$F_n = \frac{2G}{3(1-v)} {R_e}^{1/2} \delta^{3/2} \tag{3}$$

where

G = the shear modulus of the spheres,
ν = the Poisson ratio of the spheres, and

R_e = $R_1R_2/(R_1 + R_2)$, where the radius for each grain, R_1 and R_2, is equal to the radius of a sphere of volume equal to the grain volume.

Coulombic frictional forces act between each grain pair. The frictional contact force, F_t, at time m is calculated incrementally from the force at the previous time step $m - 1$ as

$$\bar{F_t}^{m} = \bar{F_t}^{m-1} - \left[k_t \Delta t \left(\bar{V}_{\frac{1}{2}} - \bar{V}_{\frac{1}{2}} \cdot \hat{n}\right)\right] \tag{4}$$

where

k_t = the tangential contact stiffness,
$\hat{n}$ = the contact normal direction, and
Δt = the time step.

The dependence of the tangential stiffness on the normal force (Lin and Ng 1997) is

$$k_t = \frac{2[3G^2(1-v)F_nR_e]^{1/3}}{2-v}. \tag{5}$$

The tangential force is also damped. Once the frictional force, F_t, exceeds the Coulomb limit, sliding at the grain interface begins. This can be written as follows:

$$\text{if } \left|\bar{F_t}^{m+1}\right| > \mu {F_n}^{m+1}, \text{then } \left|\bar{F_t}^{m+1}\right| = \mu {F_n}^{m+1} \tag{6}$$

where μ is the coefficient of friction. The tangential contact force (using Equation [4]) is calculated incrementally to account for changes in the direction of the tangential component of the relative velocity and changes that the normal contact force produces in the tangential stiffness.

After the contact and body forces on each soil grain are calculated, the equations of motion are solved for new positions and velocities; and time advanced one step using a Leapfrog integration scheme, which is second order accurate in time and is conservative. During the simulation, the time step is adjusted dynamically using the equation

$$\Delta t = \frac{\pi}{10}\sqrt{\left(\frac{M}{k_{eff}}\right)_{min}} \tag{7}$$

where M is the mass of the smaller of the two grains in a contact and the effective contact stiffness, k_{eff}, is

$$k_{eff} = \frac{2\sqrt{2}G}{3(1-v)}{R_e}^{1/2}\delta^{1/2}. \tag{8}$$

During each simulation, the energy balance is calculated to verify the self-consistency of the simulation. The components of the energy balance are work performed on the grains, the change in the kinetic and potential energy of the grains, inelastic dissipation, frictional dissipation, and viscous drag losses.

3.2 Triaxial shear experiment

During projectile penetration, energy is transferred from the projectile through the target material via wave propagation. For unconsolidated granular media, wave propagation is fundamentally the transfer of kinetic energy from one particle to another through compression and shear. The bulk material properties, such as the elastic and shear moduli, are simply the collective product of a number of particle interactions and, therefore, can be estimated a priori with the formulation of appropriate contact laws that incorporate the effects of liquid water to account for moisture in the target material.

Work on the contact behavior of dry grains (Cole et al. 2013) has shown that the initial state of force at the contacts due to the soil-fabric microstructure and overburden pressure determine the dynamic stiffness and attenuation for that material. The near-surface wave propagation and attenuation in moist soils depend not only on these factors but also on saturation level, pore geometry, and encapsulated air. To examine the effects of varying levels of moisture on the dynamic behavior of a soil, we fabricated a small-scale triaxial shear test. The results from these experiments were used to inform the DEM contact model development and subsequent calibration. As described above, the forces at the particle-to-particle interface in the DEM model are parameterized by a shear modulus, friction coefficient, and damping coefficient. We can then use the experimental results of the triaxial shear experiments to estimate the value of these parameters, plug these values into the numerical model, and use the difference between the simulated behavior and the observed behavior to improve our parameter estimation. This workflow can then be repeated for varying soil conditions (i.e., moisture contents) to parameterize the soil's mechanical properties by moisture content.

3.2.1 Experimental setup and procedure

The triaxial shear test setup was composed of a linear piezoelectric actuator that cyclically loaded a granular sample and a load cell that recorded the sample's response to loading (Figure 1).

Figure 1. Diagram of triaxial shear test setup with a granular sample. This entire setup sits inside of a pressure vessel.

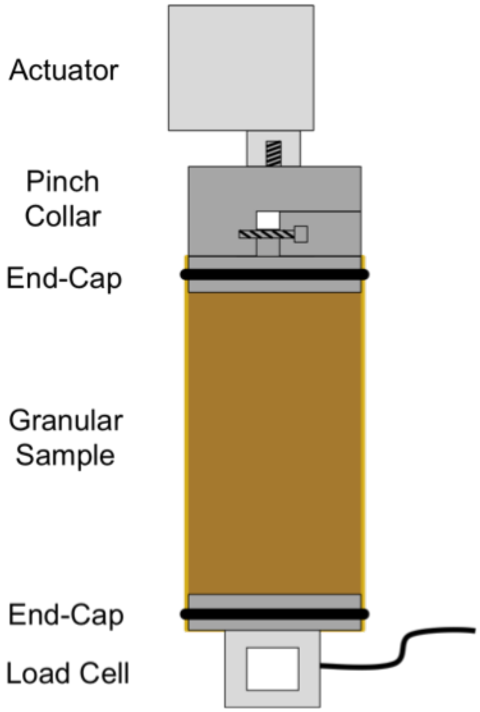

Test samples consisted of American Society for Testing and Materials (ASTM) 20-30 standard test sand contained in latex membranes, which maintained the sample's form and moisture content while allowing the vessel's pressure to confine the granular material. ASTM 20-30 sand is a smooth-grained quartz sand that is predominantly graded to pass through a 850 µm (No. 20) sieve and be retained by a 600 µm (No. 30) sieve (ASTM International 2013). Samples were approximately 36 mm in diameter and 85 mm in length and were moistened with a 25% potassium iodide solution (by weight). The ends of the samples were enclosed by aluminum platens that connected to the actuator and load cell. Rubber O-rings sealed the latex membrane to the aluminum platens.

The actuator's loading signal followed a haversine produced by a computer-controlled function generator. The loading signal was limited so that the resultant sample displacement was less than 500 nm peak-to-peak and the frequency was less than 150 Hz (i.e., cycles per second). The actuator contained a strain gauge, which measured the amount of strain experienced by the granular sample.

Sample moisture contents varied between dry and fully saturated (~10%) (Note: for these initial results, the "dry" sample material was not baked to remove all moisture). Samples were formed within a mold to ensure consistent sample shape and size across all tests. Samples were prepared by measuring the amount of material needed to fill the mold and then adding the appropriate amount of water to achieve each desired moisture content level. The material was mixed with the water, inserted into the latex membrane, compacted into the mold, and then placed inside the testing apparatus.

Once the samples were properly aligned in the setup, the mold was removed; and a standard preloading scheme was applied to initialize the material to a state that was consistent, or as close to consistent as possible, across all samples. Once the standard initial state was achieved, the sample was cyclically compressed in the axial direction for frequencies ranging from 10 to 150 Hz for a constant amplitude. The actuator was controlled using a displacement-following feedback loop to ensure that the amplitude was in fact held constant over all the forcing frequencies tested.

3.2.2 System dynamics model

The contact between DEM grains is modeled using a modified Hertzian contact model, which is a nonlinear viscoelastic contact model. The system dynamics of the triaxial shear experimental setup can be modeled in a similar manner as the DEM model to provide an analog between the numerical and physical experiments. Assuming frequency-invariant stiffness and damping of the experimental system, the measured force, F, is

$$F = kx + b\dot{x} \tag{9}$$

where k, b, x, and $\dot{x}$ denote the stiffness, damping, displacement, and displacement rate, respectively. The sample is subjected to a harmonic displacement such that the load and displacement take the following forms:

$$F = F_0\cos(\omega t) \tag{10}$$

and

$$\begin{gathered} x = x_0\cos(\omega t + \phi) \\ \dot{x} = -x_0\omega\sin(\omega t + \phi) \end{gathered} \tag{11}$$

where ϕ is the phase lag and ω is the angular frequency, which is equal to 2π times the load signal frequency, f. F_0 and x_0 are load and displacement amplitudes. A phase difference between the displacement and load signals is assumed. Substituting Equations (10) and (11) into (9) returns

$$F_0\cos(\omega t) = kx_0\cos(\omega t + \phi) - bx_0\omega\sin(\omega t + \phi), \tag{12}$$

which can be simplified with the following trigonometric identities,

$$\begin{gathered} \cos(\alpha + \beta) = \cos(\alpha)\cos(\beta) - \sin(\alpha)\sin(\beta) \\ \sin(\alpha + \beta) = \sin(\alpha)\cos(\beta) + \cos(\alpha)\sin(\beta), \end{gathered} \tag{13}$$

and rearranged such that

$$\begin{gathered} [F_0 - kx_0\cos(\phi) + bx_0\omega\sin(\phi)]\cos(\omega t) + [kx_0\sin(\phi) \\ + bx_0\omega\cos(\phi)]\sin(\omega t) = 0. \end{gathered} \tag{14}$$

For Equation (14) to hold true, the bracketed terms must both be independently equal to zero:

$$\begin{gathered} F_0 - kx_0\cos(\phi) + bx_0\omega\sin(\phi) = 0 \\ kx_0\sin(\phi) + bx_0\omega\cos(\phi) = 0 \end{gathered} \tag{15}$$

These can then be used to solve for k and b:

$$k = \frac{F_0 \cos(\phi)}{x_0}$$
$$b = \frac{-k}{\omega} \tan(\phi) \tag{16}$$

To extract the elastic and viscous components of the granular samples, we must first determine the dynamic contributions from the experimental setup itself. The system's stiffness and damping were measured by placing a steel sample within the setup and using Equation (16) to calculate k and b for the measured results. It was assumed that the steel sample's stiffness and damping were much larger and lower, respectively, than those of the system.

We then assumed that the stiffness and damping components for the system combine linearly with those of the sample such that the total system dynamic response is

$$F_{sys} = \big(k_s + K_m(f)\big)x + \big(b_s + b_m(f)\big)\dot{x} \tag{17}$$

where the subscripts s and m refer to the experimental setup and granular material responses to dynamic loading, respectively. This way, the dynamic responses of both the granular sample and experimental setup can be separated from one another.

3.3 Projectile-drop test

Ultimately, the numerical modeling developed in this effort will be used to predict the penetration behavior and final depth for a given projectile, impact conditions, and soil conditions. A companion effort was used to calibrate the DEM model and to validate the DEM modeling approach, which involved several drop tests into dry and wet uncompacted ASTM 20-30 test sand using 3-dimensional printed replicas of a 57 mm M70 projectile. Two projectiles were used for the drop tests: one full-sized projectile measuring 170 mm in length, 56.78 mm in diameter, and weighing 409.64 g and one half sized projectile 85.05 mm in length, 28.35 mm in diameter, and weighing 51.19 g.

The impact material was contained in a box measuring 30 cm long, 15 cm wide, and 30 cm high. The projectiles were dropped from a height of 24 in. for each test and were allowed to free fall into the sand bed. For the dry sand tests, the diameter of the indention was measured and recorded; then the impact crater was filled with new dry sand and smoothed over between each drop. For the wet sand tests, water was added to the drop area by using a bottle mister before each drop. The diameter of the indention was measured and recorded; then a sample of sand was taken and weighed to determine the moisture content at the impact site for each drop. The drop tests were video recorded at 389 frames per second so that the projectile position and velocity as a function of time could be estimated directly from the frame-by-frame displacement.

3.4 Coupling the finite element method with the discrete element method

To reduce the overall computational complexity of the modeling effort, a continuum domain was used to approximate the discrete particle domain in the far field. This is done because the computational cost of modeling the entire domain with only discrete particles would be very computationally expensive. In the near field, the soil was modeled using the DEM and approximated as spherical particles. The size of the domain that contains the spherical particles was chosen to be large enough such that penetration of the projectile into the soil is not influenced by the continuum boundary (e.g., influence from reflecting pressure waves at the boundary). To model the continuum in the far field, the open source deal.II (Bangerth et al. 2007) finite element method (FEM) library is used. The two types of models (FEM and DEM) interact through a coupling surface, which is defined on any part of the finite element domain that could come into contact with particles. The next subsections describe the continuum domain physics, closest contact point determination, and interaction physics at the coupling surface, which are all pertinent to the coupling of the finite element and discrete element codes.

3.4.1 Quasi-static linear elasticity

In the far-field domain of the penetration model, we approximate the soil as a linear elastic continuum and use FEM to solve the system. Linear elasticity is a poor representative material model for a real soil, but we have used a linear elastic constitutive model in lieu of a constitutive model that includes plasticity (e.g., Mohr-Coulomb) to simplify the coupling scheme and to reduce computational cost in this early developmental stage.

The equations of motion that represent the physics of the continuum domain can be seen in Equation (18) where σ is the Cauchy stress, F is a body force (e.g., gravity), ρ is density, and a is the acceleration. We assume that the influence of inertia, or dynamics, in this problem is small; so the acceleration is set to zero:

$$\nabla \cdot \sigma + F = \rho a = 0 \tag{18}$$

We further assume that in the continuum, the soil behaves as an isotropic linear elastic body according to the constitutive law

$$\sigma = C : \varepsilon \tag{19}$$

where C is the fourth order elasticity tensor and ε is the strain. We assume that small-strain theory is appropriate for the continuum domain as we expect the deformation to be small in this region. Using the small-strain assumption, the strain tensor is

$$\varepsilon = \frac{1}{2}(\nabla u + (\nabla u)^T) \tag{20}$$

where u is the displacement and T denotes the transpose of the gradient tensor ∇u. To solve Equation (18), we multiply the equation by a test function, w, and integrate by parts to get the weak form of the equations of motion

$$\int_\Omega \nabla w : \sigma d\Omega = \int_\Omega w \cdot F d\Omega + \int_\Gamma w \cdot t d\Gamma \tag{21}$$

where the integral over Γ is the part of the domain where a traction t is applied. For our purposes, the traction t will be the load applied by a spherical particle when it contacts the coupling surface on the continuum domain. Dirichlet, or fixed, boundary conditions are applied to the outside of the continuum domain.

3.4.2 Closest contact point calculation

As particles travel through the domain, they will interact with each other and they will interact with the deformable continuum domain through the coupling surface. To determine if a particle is in contact with the continuum domain, the closest point between the spherical particle center and the coupling surface needs to be calculated. Because our continuum domain can deform in time and our finite elements at the coupling surface do not have to be planar, finding the closest point poses a challenge. To address this problem, we solve the constrained optimization problem

$$\min z = \|y(X) - P(x)\|^2 \text{ subject to } X \in (X_1, X_2, 1) \text{ and } X_1, X_2 \in [-1,1] \tag{22}$$

where z is the norm square distance between a point y on the coupling surface and a particle center, P. Figure 2 shows the two points and the distance between them, indicated by a dotted red line. When Equation (22) is minimized, the result will be a point y on the coupling surface that is the closest point to the spherical particle.

Figure 2. Mapping between the coupling-surface finite elements in the real space and reference space during closest-point determination. Point *P* is the spherical particle center, point *X* is the closest point on the reference element surface to the particle point *P*, and *y*(*X*) is the mapping of point *X* onto the real space.

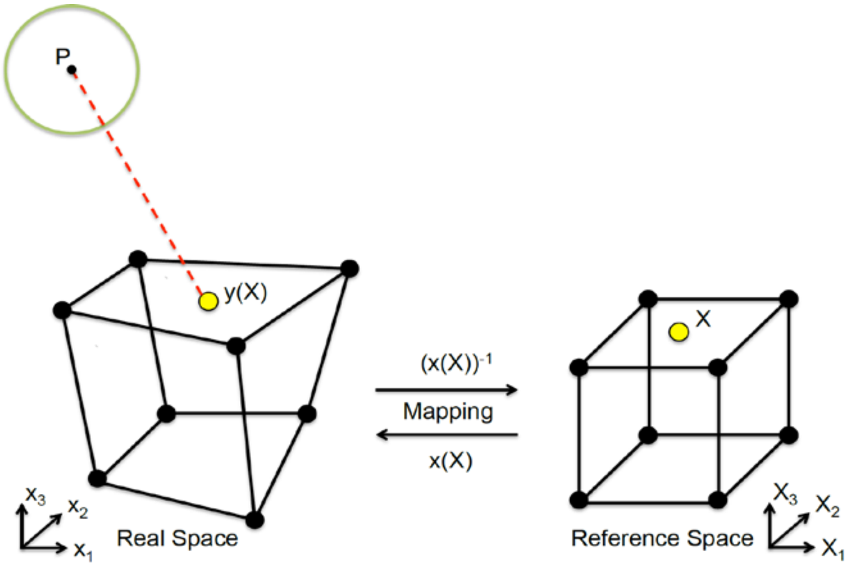

To avoid the difficulties of finding the closest contact point on the deformed element, we pose that there exists a point on a reference element that can be mapped onto the real space. The mapping from point X in the reference space to point y in the real space is

$$y(X) = \sum_I N_I(X) x_I \tag{23}$$

where

N_{I} = the Lagrange interpolation functions,
x_{I} = the coordinates of the element nodes in the real space, and
I = the element node number.

For the three dimensional problem we consider, the summation over I runs from 1 to 8. In our optimization problem, we constrain our minimization statement by ensuring that the point X in the reference space lies in the top surface ($X_1 \in [-1, 1]$, $X_2 \in [-1, 1]$, $X_3 = 1$). To find the minimum of Equation (22), we take the gradient of z and set it equal to zero

$$\nabla_X z = 2\nabla_{\mathrm{x}} y \cdot (y - P) = 0; \tag{24}$$

and we iteratively find the solution, X, to this equation using the Newton-Raphson method

$$X^{n+1} = X^{n} - (\nabla_X^2 z)^{-1} \nabla x^{z} \tag{25}$$

where n refers to an iteration step and ∇_X implies that we are taking the gradient with respect to the reference coordinates. After the iteration procedure and the residual is minimized, if the closest point is located within the bounds of the element, nothing has to be done; and the solution is minimized. If the closest point lies outside the bounds of the reference domain, an additional procedure is performed that snaps the point X to the nearest point, which could be on a line segment or a corner. In our code, the closest point is calculated for each element in a subset of the total coupling surface for computational efficiency. The results of such a procedure can been seen in Figure 3. For this effort, we consider single point-wise interaction per particle, so the closest particle–surface pair is stored. If the closest-point vector has a magnitude larger than the particle radius, nothing has to be done; and the simulation marches forward. On the other hand, if the magnitude of the closest-point vector is smaller than the radius of the particle, contact is detected; and an additional procedure needs to be completed, which is explained in the next subsection.

Figure 3. Potential results of an element-wise closest-point calculation on the coupling surface with the *red segmented line* showing the closest point.

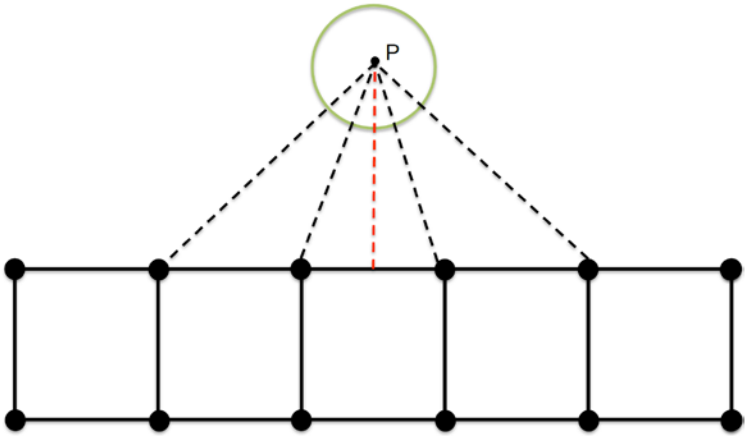

3.4.3 Finite element and discrete particle interaction physics at the coupling surface

The coupling surface is the portion of the continuum domain that couples the movement of the spherical particles to the deformation of the continuum. At this interface, forces are transferred to and from each domain during particle–continuum contact, which is detected when the magnitude of the closest-point vector is less than the particle radius. As shown in Figure 4, the particle is penetrating the finite element at a distance of δ, which can be calculated by taking the difference between the magnitude of the closest-point vector and the particle radius.

Figure 4. A spherical particle penetrating a deformable continuum finite element at the coupling surface. The nearest contact point is indicated by the *dashed red line*, the depth of indentation δ is indicated by the *dashed blue line*, and R is the particle radius.

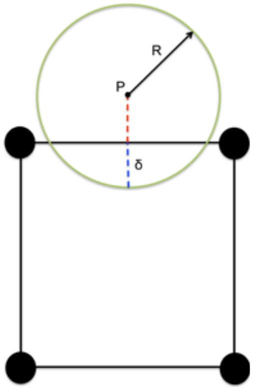

The contact force generated on the continuum surface during impact is defined as

$$P_i = K\delta_i \tag{26}$$

where

P_i = the force from the particle impact,
K = the stiffness of the particle,
δ_i = the penetration distance, and
i = the particle number in the interaction.

The number of particles interacting with the boundary can vary throughout a simulation. The particle impact force P_i is applied to the continuum body through the equation

$$F = \sum_i P_i \int_\Gamma w \cdot \delta(x - p_i) d\Gamma \tag{27}$$

where

F = the force vector acting on the coupling surface,
w = the test function,
$\delta(x - p_i)$ = a delta function,
p_i = the closest contact point on the coupling-surface element, and

the sum is over the number of particle contacts. This vector F and the body force vector are added together and are what drive the deformation of the continuum body. On the DEM side of the code, an equal and opposite force (to the one applied to the coupling surface) is applied to the particle to drive the acceleration of the particle away from the boundary.

4 Results and Discussion

4.1 Triaxial shear test

Recall that the particle-to-particle interactions can be described by the grain-scale elastic modulus (or shear modulus, which is a function of the elastic modulus and Poisson's ratio), viscous damping coefficient, and the friction coefficient. A granular material's bulk properties, such as elastic modulus and viscous damping coefficient, are a result of the individual particle-to-particle interactions in aggregate. Therefore, if we can extract the bulk elastic modulus and the damping coefficient from a sample's mechanical response to small-strain cyclical loading by using the triaxial shear test and the dynamical system formulation described in Section 3.2.2, then we can then infer the particle-scale parameters that govern the bulk constitutive behavior. We highlight that the soil samples were tested with no applied confining stress, resulting in weaker coupling between neighboring soil grains.

In this set of experiments, the forcing amplitude (i.e., the maximum axial strain) was kept constant for frequencies ranging from 10 to 150 Hz. Figure 5, the triaxial shear test results, shows that the sample's spring stiffness, which is directly proportional to the elastic modulus, generally decreases as the forcing frequency increases (i.e., the material exhibits "softer" elastic behavior where it does not recover to its original state as quickly). Because the particle velocity increases with frequency, the relative velocity between particles also increases and leads to sliding at the interface. This scenario appears to be corroborated by the decrease in stiffness when moisture is added to the system where the water is lubricating the particle interface, allowing more sliding to occur.

The viscous damping coefficient also decreases with increasing frequency (Figure 5) until reaching a nearly constant value for frequencies above 30–40 Hz, which at first is a bit puzzling if sliding is the mechanism for the stiffness decrease with increasing frequency (i.e., strain rate). But in our viscoelastic model of the sample dynamics (Equation [16]), the damping coefficient, b, is proportional to the stiffness, k. Therefore, if the ratio of the tangent of the phase lag angle, $\tan(\phi)$, and the forcing frequency, ω, is either constant or slowly varying with frequency, then the damping coefficient would decrease.

Figure 5. Granular sample stiffness (*k*) and damping coefficients (*b*) for various initial moisture contents. The material stiffness and damping coefficients decrease with increasing frequency and moisture content. For the frequency range considered, the damping coefficient does not vary with moisture content in a in a discernable manner; however, the stiffness transitions to a state with higher magnitude when the moisture content is negligible.

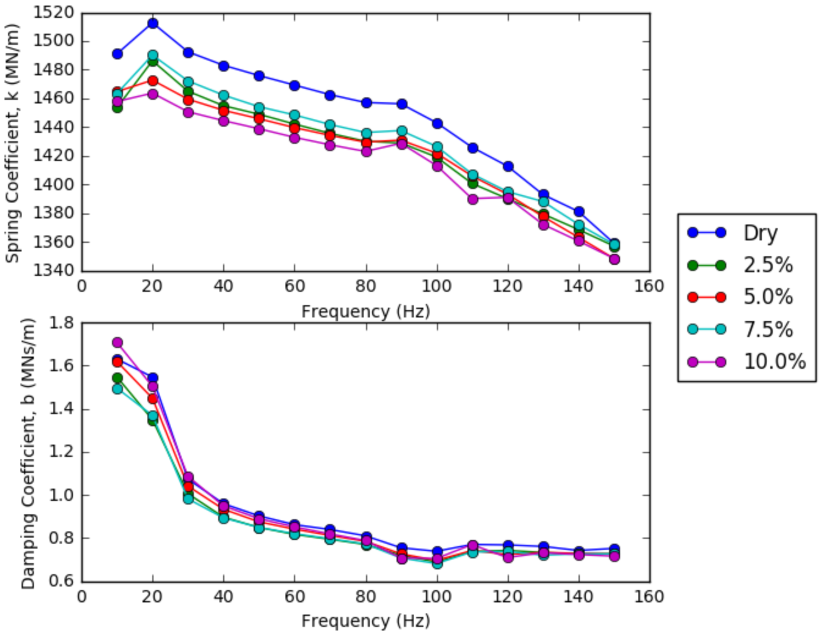

4.2 Projectile-drop test—physical experiments

The results of these projectile-drop experiments will provide the data needed to validate the numerical model effort. As described previously, the projectile was dropped from a height of 0.61 m from the sand bed surface. Figures 6 and 7 illustrate the projectile just before penetration, at midimpact, and when the projectile has reached its maximum depth for dry and moist conditions. The impact velocities (i.e., the projectile velocities at t = 0.0 in Figure 8) range from 3.1 to 3.5 m/s, which is in relatively good agreement with the theoretical impact velocity of 3.5 m/s of a body accelerating due to gravity from an initial height of 0.61 m.

For each size projectile (full- and half-scale projectile models) and particle-bed conditions (dry and 2.3% moisture content by weight), the penetration process can be divided into three stages. In the first stage, there is a roll off of the velocity (as seen in Figure 8) as the projectile first enters the particle bed; and the deceleration is gradual as the particles at the surface provide little resistance to the entering projectile. As the projectile travels farther into the particle medium, the deceleration reaches a maximum (the location of the peak impact force in Figure 9). The final stage is the period after the maximum impact force has been reached until the projectile has come to rest. The magnitude difference in impact force between the full-scale and half-scale projectiles is predominantly due to the mass difference between the two sizes, where the half-scale projectile mass is 13% the value of the full-scale model.

Figure 6. Projectile model entering dry sand. The images are taken from the moment of impact (*t* = 0), at mid-impact, and when the projectile has reached its final depth.

(a) *t* = 0 seconds

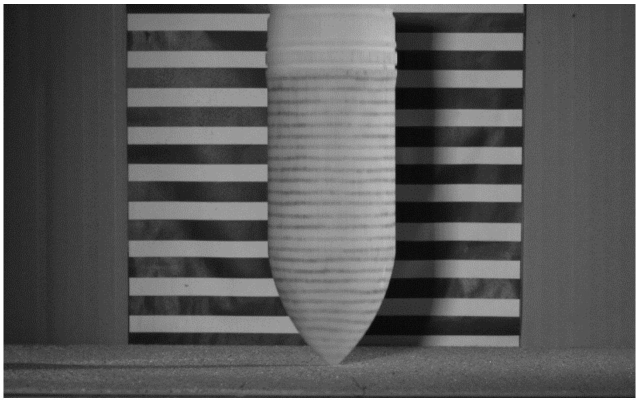

(b) *t* = 0.2 seconds

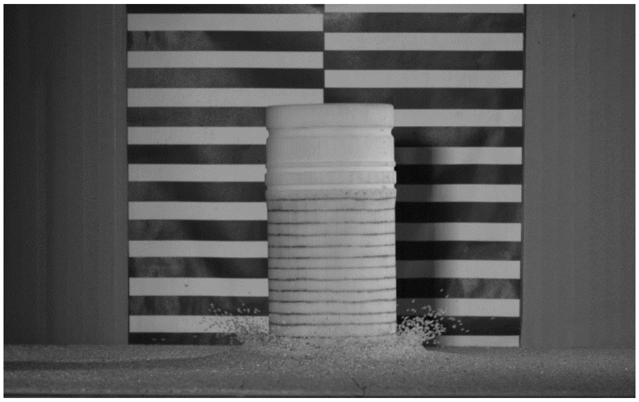

(c) *t* = 0.4 seconds

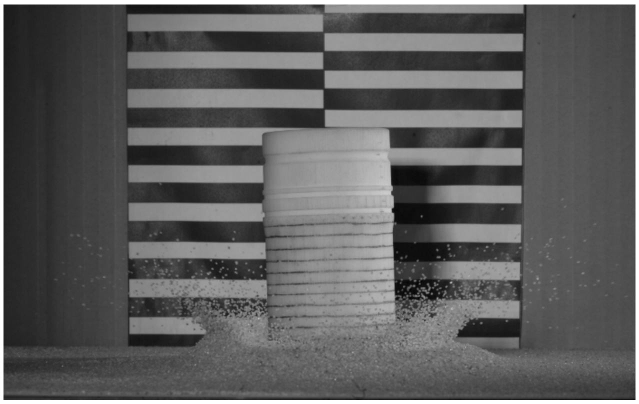

Figure 7. Projectile entering moist sand. Similar to the dry sand images, the frames are taken from the moment of impact ($t = 0$), at mid-impact, and when the projectile has reached its final depth. Note how the crater formation is less pronounced as compared to the dry particle bed.

(a) $t = 0$ seconds

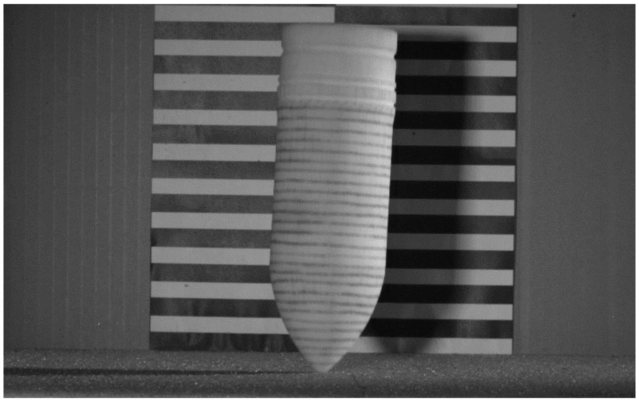

(b) $t = 0.2$ seconds

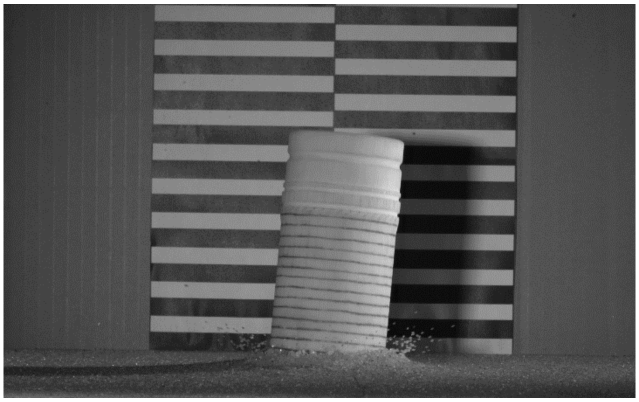

(c) $t = 0.4$ seconds

Figure 8. Measured projectile velocities.

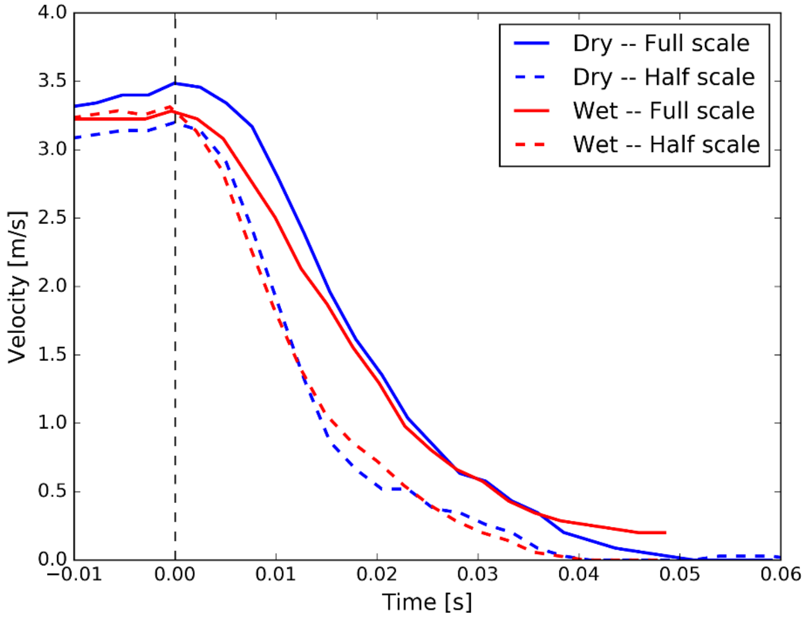

Figure 9. Measured impact forces.

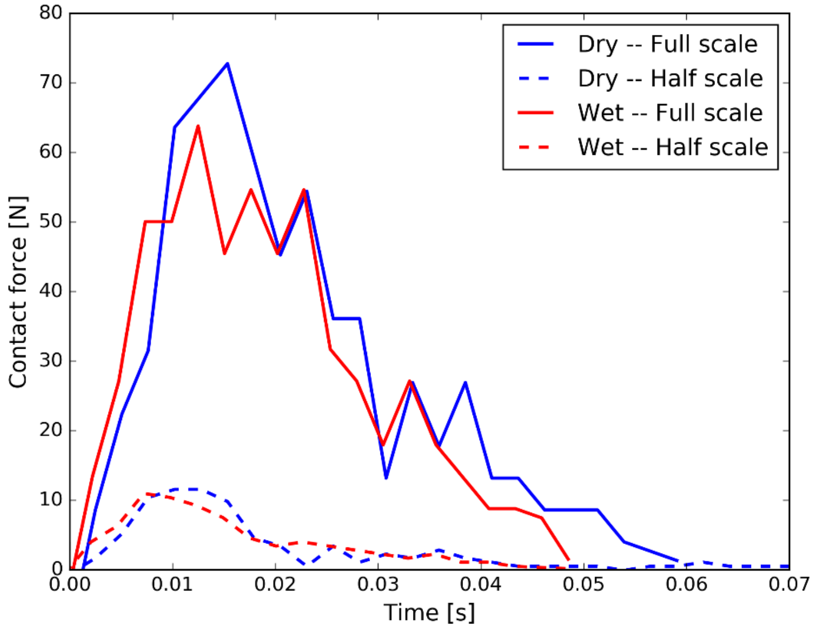

There is no observable difference in penetration behavior between the dry and wet cases for both the full- and half-scale models, likely due to the projectile's low impact velocity, therefore kinetic energy, and the small change in soil bulk density with the addition of moisture at 2.3% by weight.

4.3 Projectile-drop test—numerical model

The numerical companion to the penetration drop test described above was performed to demonstrate the feasibility of coupling laboratory measurements with numerical model development and calibration. Table 1 lists the simulation parameters. We selected the numerical simulation values to ensure stability rather than a one-to-one match. Future work will include improvements to the numerical model to enable direct comparison between the model and experiments.

The preliminary numerical model results compare well in a qualitative sense with the drop-test measurements. The temporal evolution of the impact forces, plotted for the numerical model in Figure 10, exhibits the rapid initial rise in contact forces as the projectile enters the particle bed and reaches a peak contact force of 350 kN after which the impact force decreases at a rate slower than the initial rise. The impact forces in the numerical simulation show pronounced high-frequency fluctuations that are due to the relatively small number of grains that are in contact with the projectile at any one time, as seen Figure 11, which amplifies the effect that any one grain has on the projectile. We do observe the development of a pressure bulb around the projectile tip (in Figure 11) although not as pronounced due to the small number of grains in the simulation. Again, we anticipate correlation between numerical and physical experiments to improve as we increase the number of grains while also bringing the mechanical properties of the simulated material to match the real material.

Table 1. DEM simulation parameters.

Parameter	Value
Projectile mass	10 kg
Projectile diameter	57 mm
Grain mass	1.0 g
Grain diameter	5 mm
# of grains	50×10^3
Shear modulus	10^9 Pa
Poisson’s ratio	0.4
Time step	10^{-5} s
Impact velocity	2.0 m/s

Figure 10. Time trace of impact forces estimated from the DEM simulation of the projectile-drop test. The time evolution of the penetration forces on the projectile compare well in a qualitative sense.

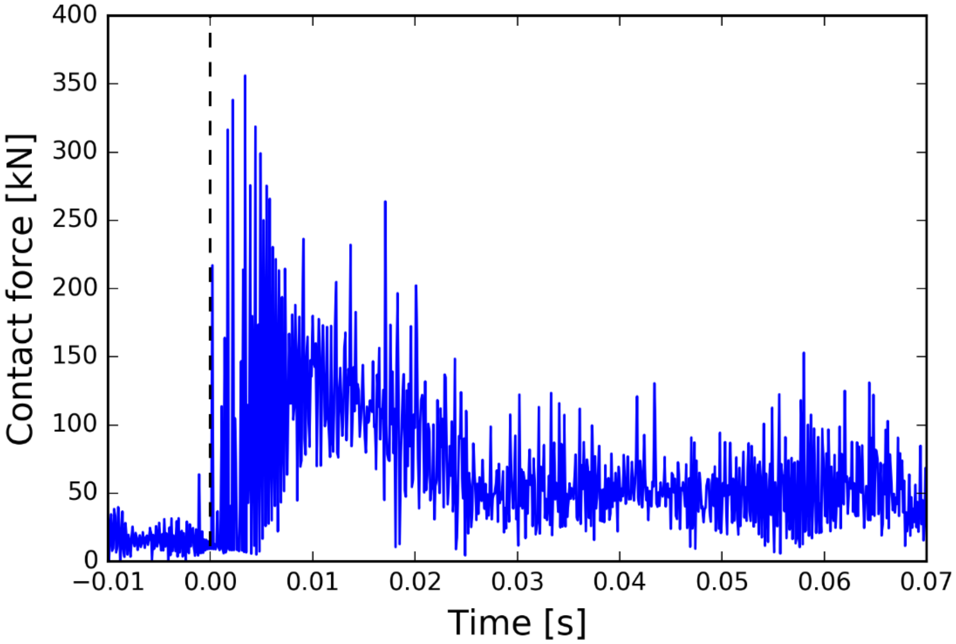

Figure 11. DEM simulation of the projectile-drop experiment. Example frame from the DEM simulation showing the development of the pressure bulb at the tip of the projectile. The contact-force-magnitude units are Newtons.

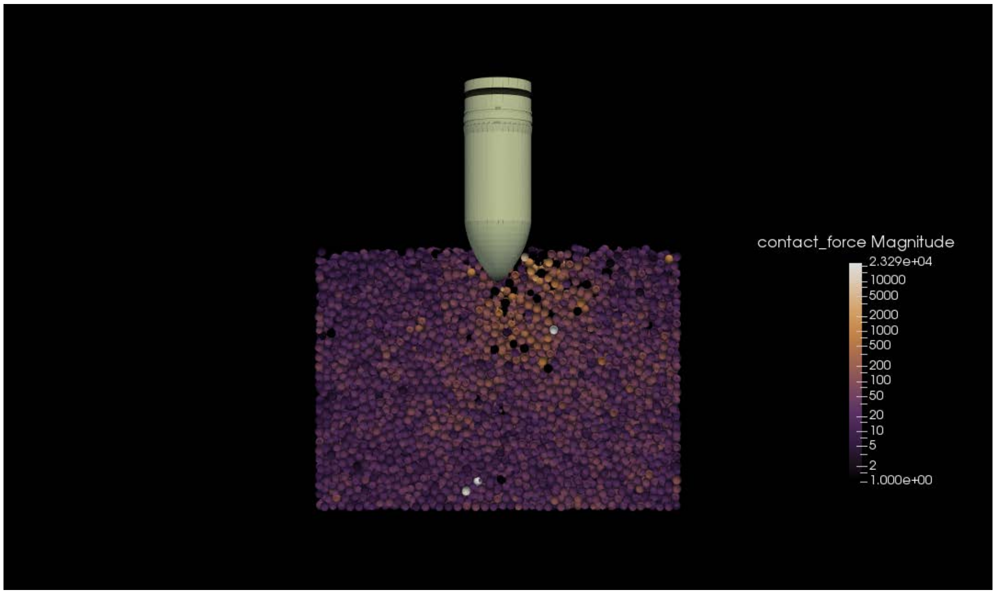

5 Conclusions and Implications for Future Research

The work presented in this report demonstrates a framework that would improve projectile penetration models by enabling the development of better constitutive models that depend on only the parent material characteristics (elastic modulus, Poisson's ratio), the grain geometry, the friction coefficient, and the volume of pore water. Of these parameters, the friction coefficient is the least known for a particular soil type. The triaxial shear test experiments, which characterize the dynamic behavior and transfer of energy through the soil fabric, serve as a good source of data to calibrate the friction coefficient. Comparison with the drop test, and eventually gas gun tests, are the basis for model validation.

5.1 Triaxial shear test—numerical model

The friction coefficient calibration would be through direct comparison between the physical experiments and numerical model simulations of the same particle configurations and forcing conditions. The DEM model particle configurations would be generated from three-dimensional microCT imaging of a soil sample of interest (Figure 12) and subject to the same unsteady forcing to calibrate the friction coefficient such that the dynamic behaviors match.

Figure 12. Using three-dimensional microCT imaging to generate realistic particle geometries. CRREL in-house capabilities include a high-energy microCT scanner that is capable of imaging resolutions up to 10 *μm*. Segmentation methods are in development to extract particle geometries as triangulated surface meshes, as seen in (*a*), as well as pore water distribution and liquid bridge geometries.

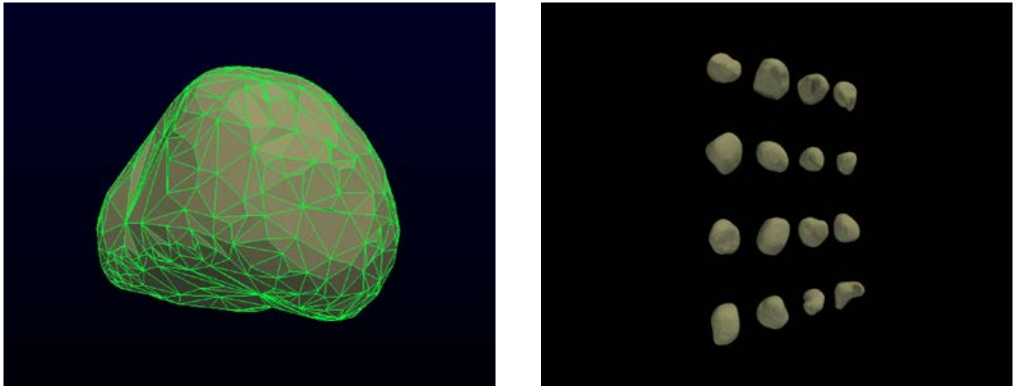

(a) Detail of particle surface discretization.

(b) Sample of several particle geometries generated from microCT scans.

5.2 Coupled DEM and FEM penetration model

As this work continues, we plan to couple a nonlinear, finite-strain, explicit-dynamics, finite element code to the discrete element code. This will give us the ability to capture more dynamic and impulsive loads on a continuum body. We also plan to extend our constitutive modeling capabilities to include nonlinear material models such as J_2 plasticity. As we refine our code, we continue to look at ways to improve the computational speed of the coupling-surface identification, closest-point determination, and contact-detection algorithms to be able to model larger domains.

5.3 Final thoughts

The advantage of a micromechanical approach to the projectile penetration problem is the potential predictive power once the material's parent materials and interaction behavior (e.g., moisture effects and friction between grains) are determined. The projectile penetration-depth prediction then moves beyond empirical correlations that are tightly tied to the conditions and soil characteristics of the test, thus lacking generality, to a model that can predict penetration depth based on quantities that are easily measured in a controlled laboratory setting. This approach will ultimately reduce the uncertainty in penetration-depth predictions and in turn reduce MEC remediation costs.

References

Allen, W. A., E. B. Mayfield, and H. L. Morrison. 1957. Dynamics of a Projectile Penetrating Sand. *AIP Journal of Applied Physics* 28 (3): 370–376.

ASTM International. 2013. C778-92a: Standard Specification for Standard Sand. *Annual Book of ASTM Standards,* Section 4, 329–31.

Bangerth, W., R. Hartmann, and G. Kanschat. 2007. deal.II—A General-Purpose Object-Oriented Finite Element Library. *ACM Transactions on Mathematical Software* 33 (4): 24.

Bernard, R. S. 1977. *Empirical Analysis of Projectile Penetration in Rock*. Miscellaneous Paper S-77-16. Vicksburg, MS: U.S. Army Engineer Waterways Experiment Station.

———. 1978. *Depth and Motion Prediction for Earth Penetrators*. Technical Report S-78-4. Vicksburg, MS: U.S. Army Engineer Waterways Experiment Station.

Bernard, R. S., and D. C. Creighton. 1978. *Projectile Penetration in Soil and Rock: Analysis for Non-Normal Impact*. Technical Report S-78-14.Vicksburg, MS: U.S. Army Engineer Waterways Experiment Station.

———. 1979. *Non-Normal Impact and Penetration: Analysis for Hard Targets and Small Angles of Attack*. Technical Report S-79-15.Vicksburg, MS: U.S. Army Engineer Waterways Experiment Station.

Bless, S., W. Cooper, K. Watanabe, and R. Peden. 2012. Deceleration of Projectiles in Sand. In *AIP Conference Proceedings 2012*, 1426:45–47.

Borg, J. P., A. Fraser, and A. Van Vooren. 2012. Ballistic Penetration of Sand with Small Caliber Projectiles. In *AIP Conference Proceedings 2012,* 1426:48.

Cole, D. M. 2015. Laboratory Observations of Frictional Sliding of Individual Contacts in Geologic Materials. *Granular Matter* 17:95–110.

Cole, D. M., and S. A. Ketcham. 2013. Dynamic and Impact Contact Mechanics of Geologic Materials: Grain-Scale Experiments and Modeling. In *AIP Conference Proceedings*, 1542:221–224.

Cole, D. M., and J. F. Peters. 2007. A Physically Based Approach to Granular Media Mechanics: Grain-Scale Experiments, Initial Results and Implications to Numerical Modeling. *Granular Matter* 9 (5): 309–321.

———. 2008. Grain-Scale Mechanics of Geologic Materials and Lunar Simulants under Normal Loading. *Granular Matter* 10:171–185. doi: 10.1007/s10035-007-0066-y.

Cole, D. M., M. A. Hopkins, S. W. Broadfoot, and S. D. Sloan. 2013. *Dynamic Contact Mechanics of Geologic Materials: Experiments, Modeling and Applications,* 467–474. New York: Springer New York.

Evans, D. J., and S. Murad. 1977. Singularity Free Algorithm for Molecular Dynamics Simulation of Rigid Polyatomics. *Molecular Physics* 34:327–331.

Forrestal, M. J. 1986. Penetration into Dry Porous Rock. *International Journal of Solids Structures* 22:1485–1500.

Forrestal, M. J., J. D. Cargile, and R. D. Y. Tzou. 1992. Penetration of Concrete Targets. SAND-92-2513c. Albuquerque, NM: Sandia National Laboratory.

Hardin, B. O., and V. P. Drnevich.1972. Shear Modulus and Damping in Soils: Design Equations and Curves. *Journal of the Soil Mechanics and Foundation Division (ASCE)* 98:667–692.

Hardin, B. O., and F. E. Richart. 1963. Elastic Wave Velocities in Granular Soils. *Journal of the Soil Mechanics and Foundation Division* 89:33–65.

Iwasaki, T., F. Tatsuoka, and Y. Takagi. 1974. Shear Moduli of Sands under Cyclic Torsional Shear Loading. *Soils and Foundations* 18:39–56.

Johnson, K. L. 1987. *Contact Mechanics*. Cambridge, UK: Cambridge University Press.

Lin, X., and T.-T. Ng. 1997. A Three-Dimensional Discrete Element Model using Arrays of Ellipsoids. *Geotechnique* 47:319–329.

Richart, F. E., J. R. Hall, and R. D. Woods. 1970. *Vibrations of Soil and Foundations*. Englewood Cliffs, NJ: Prentice-Hall Inc.

Seed, H. B., R. T. Wong, I. M. Idriss, and K. Tokimatsu.1986. Moduli and Damping Factors for Dynamic Analyses of Cohesionless Soils. *Journal of Geotechnical Engineering* 112:1016–1032.

Shi, C., M. Wang, J. Li, and M. Li. 2014. A Model of Depth Calculation for Projectile Penetration into Dry Sand and Comparison with Experiments. *International Journal of Impact Engineering* 73:112–122.

Tatsuoka, F., T. Iwasaki, and Y. Takagi. 1978. Hyseretic Damping of Sands under Cyclic Loading and Its Relation to Shear Modulus. *Soils and Foundations* 18:25–40.

Young, C. W. 1967. *The Development of Empirical Equations for Predicting Depth of an Earth-Penetrating Projectile*. SC-DR-67-70. Albuquerque, NM: Sandia National Laboratory.

———. 1997. *Penetration Equations*. SAND97-2426. Albuquerque, NM: Sandia National Laboratory.

REPORT DOCUMENTATION PAGE

Form Approved
OMB No. 0704-0188

1. REPORT DATE *(DD-MM-YYYY)*
August 2017

2. REPORT TYPE
Technical Report/Final

3. DATES COVERED *(From - To)*

4. TITLE AND SUBTITLE
Munition Penetration-Depth Prediction: SERDP SEED Project MR-2629

5a. CONTRACT NUMBER

5b. GRANT NUMBER

5c. PROGRAM ELEMENT NUMBER

6. AUTHOR(S)
Arnold J. Song, Brendan A. West, Oliver-Denzil S. Taylor,
Devin T. O’Connor, Matthew D. Parno, Taylor S. Hodgdon, David M. Cole, and
Jay L. Clausen

5d. PROJECT NUMBER
MR-2629

5e. TASK NUMBER

5f. WORK UNIT NUMBER

7. PERFORMING ORGANIZATION NAME(S) AND ADDRESS(ES)

U.S. Army Engineer Research and Development Center (ERDC)
Cold Regions Research and Engineering Laboratory (CRREL)
72 Lyme Road
Hanover, NH 03755-1290

8. PERFORMING ORGANIZATION REPORT NUMBER
ERDC/CRREL TR-17-12

9. SPONSORING / MONITORING AGENCY NAME(S) AND ADDRESS(ES)
Strategic Environmental Research and Development Program
4800 Mark Center Drive, Suite 17D08
Alexandria, VA 22350-3605

10. SPONSOR/MONITOR’S ACRONYM(S)
SERDP

11. SPONSOR/MONITOR’S REPORT NUMBER(S)

12. DISTRIBUTION / AVAILABILITY STATEMENT
Approved for public release; distribution is unlimited.

13. SUPPLEMENTARY NOTES

Strategic Environmental Research and Development Program (SERDP)

14. ABSTRACT

Existing models for predicting the penetration depth of munitions and explosives of concern are inaccurate and insufficient from a user (range manager, U.S. Army Corps of Engineers project manager, or environmental consultant) operability perspective for current needs. We attribute poor model performance to (1) a heavy dependence on empirically derived parameterizations poorly linked to the physical properties of the target material or (2) physics-based models that inadequately capture the salient mechanical processes, especially in the first meter of penetration. Consequently, we have developed a micromechanical-based model using a hybrid discrete element model (DEM) / finite element model (FEM) approach capable of a detailed treatment of near-surface soil properties. To examine the effects of varying levels of moisture on the dynamic behavior of a soil, we fabricated a small-scale triaxial shear test to inform the development and calibration of the DEM contact model. We conducted projectile-drop tests into sand with a scale version of a 57 mm projectile and measured projectile penetration to compare with model results.

15. SUBJECT TERMS
Discrete element method, Finite element method, Numerical analysis, Projectiles, Penetration mechanics, Prediction, Soils

16. SECURITY CLASSIFICATION OF:			**17. LIMITATION OF ABSTRACT**	**18. NUMBER OF PAGES**	**19a. NAME OF RESPONSIBLE PERSON**
a. REPORT	**b. ABSTRACT**	**c. THIS PAGE**			**19b. TELEPHONE NUMBER** *(include area code)*
Unclassified	Unclassified	Unclassified	SAR	42	

Standard Form 298 (Rev. 8-98)
Prescribed by ANSI Std. 239.18